INORGANIC CHEMISTRY FRONTIERS

RESEARCH ARTICLE

Check for updates

Cite this: *Inorg. Chem. Front.*, 2020, **7**, 505

Optical properties of undoped, Eu^{3+} doped and Li^{+} co-doped $Y_2Hf_2O_7$ nanoparticles and polymer nanocomposite films†

Santosh K. Gupta, [a,b] Jose P. Zuniga,[a] Maya Abdou,[a] P. S. Ghosh[c] and Yuanbing Mao *[d]

Received 15th September 2019,
Accepted 6th November 2019

DOI: 10.1039/c9qi01181a

rsc.li/frontiers-inorganic

Desirable phosphors for lighting, scintillation and composite films must have good light absorption properties, high concentration quenching, high quantum efficiency, a narrow color emission, and so forth. In this work, we first show that undoped yttrium hafnate $Y_2Hf_2O_7$ (YHO) nanoparticles (NPs) display dual blue and red bands after excitation using 330 nm light. Based on density functional theory (DFT) calculations, these two emission bands are correlated with the defect states arising in the band-gap region of YHO owing to the presence of neutral and charged oxygen defects. Once doped with Eu^{3+} ions (YHOE), the YHO NPs show a bright red emission, a long excited state lifetime and stable color coordinates upon near-UV and X-ray excitation. Concentration quenching is active when Eu^{3+} doping reaches 10 mol% with a critical distance of ~4.43 Å. This phenomenon indicates a high Eu^{3+} solubility within the YHO host and the absence of Eu^{3+} clusters. More importantly, the optical performance of the YHOE NPs has been further improved by lithium co-doping. The origin of the emission, structural stability, and role of Li^{+}-co-doping are explored both experimentally and theoretically. DFT calculation results demonstrate that Li^{+}-co-doping increases the covalent character of the $Eu^{3+}–O^{2-}$ bonding in the EuO_8 polyhedra. Furthermore, the YHOE NPs have been dispersed into polyvinyl alcohol (PVA) to make transparent nanocomposite films, which show strong red emission under excitation at 270 and 393 nm. Overall, we demonstrate that the YHO NPs with Eu^{3+} and (Eu^{3+}/Li^{+}) doping have a high emission intensity and quantum efficiency under UV and X-ray excitation, which makes them suitable for use as phosphors, scintillators and transparent films for lighting, imaging and detection applications.

1. Introduction

White light emitting diodes (LEDs) are among the most demanded lighting sources owing to their high power output, long-term low cost, long lifespan and environmental benignity.[1] Currently available white LEDs, which use YAG:Ce yellow phosphors combined with a blue emitting GaN semiconductor single crystal, have issues related to their high color temperature and low color rendering index.[2,3] This is mainly due to the lack of desirable red phosphors which possess a low correlated color temperature (CCT) and improved color rendering index.[4–6]

Researchers exploring and studying optical materials are continually searching for good candidates for X-ray scintillation, X-ray based luminescence deep-tissue imaging (DTI), and photodynamic therapy (PDT).[7–10] The advantage of using X-rays for DTI and PDT is that it allows deep tissue penetration, negligible X-ray scattering in tissue and negligible background for optical imaging owing to the low auto fluorescence.[11] For all these applications, single crystals, bulk ceramic materials and glasses are most commonly explored as efficient X-ray-phosphors.[7,12–15] There are lots of issues with these materials, such as the high cost and the long synthesis and processing time, the lack of optical tunability and the low scintillation efficiency.

In the phosphor library, there are efficient blue ($BaMgAl_{10}O_{17}:Eu^{2+}$) and green ($SrSi_2O_2N_2:Eu^{2+}$, $Ba_2SiO_4:Eu^{2+}$)

[a]*Department of Chemistry, University of Texas Rio Grande Valley, 1201 West University Drive, Edinburg, Texas 78539, USA*
[b]*Radiochemistry Division, Bhabha Atomic Research Centre, Trombay, Mumbai-400085, India*
[c]*Materials Science Division, Bhabha Atomic Research Centre, Trombay, Mumbai-400085, India*
[d]*Department of Chemistry, Illinois Institute of Technology, 3105 South Dearborn Street, Chicago, IL 60616, USA. E-mail: ymao17@iit.edu; Tel: +1-312-567-3815*

† Electronic supplementary information (ESI) available: Experimental information consisting of the synthesis, instrumentation and theoretical methodology, DFT calculation bond lengths, cell volumes and band gaps, XRD patterns, lattice parameters and crystallite sizes, Raman, SEM, PL decay curves (λ_{ex} = 393 nm and λ_{em} = 612 nm), plots of the decay lifetime as a function of the Eu^{3+} concentration of the YHOE NPs, lifetime values of the YHOE NPs, PL excitation spectra of the YHOE-0.5 NPs at different Li^{+} co-doping concentrations, and PL excitation spectra of the YHOE NPs at different Eu^{3+}concentrations with the same Li^{+} concentration of 2.0% for the YHOE NPs. See DOI: 10.1039/c9qi01181a

phosphors.[16,17] Finding efficient and inexpensive red phosphors is still difficult, especially those with a good thermal stability, high concentration quenching, low defect density, and so forth. One of the major problems of achieving a high emission efficiency from red phosphors designated for warm white LEDs and X-ray scintillators is their low quenching concentration of dopants.[18,19] Concentration quenching is a long-standing problem that hinders the quest for highly efficient luminescent materials. Dexter and Schulman proposed that considerable fluorescence quenching takes place in bulk materials when the activator or dopant concentration reaches 10^{-3}–10^{-2} M.[20] This problem poses serious hindrance in achieving a high luminescence intensity for their applications.

Selection of compatible hosts plays a very important role in designing desirable red phosphors. Yttrium hafnate $Y_2Hf_2O_7$ (YHO) is one of the most important pyrochlore materials for advanced technological applications such as enhancing the structural and thermal properties of metals,[21] scintillators,[22] computer tomography (CT) and positron emission tomography (PET),[23] order–disorder phase transitions,[24] and so forth. YHO is also known to exhibit excellent thermal stability, radiation stability, the ability to accommodate rare earth ions at both Y^{3+} and Hf^{4+} sites, and so on. This makes $Y_2Hf_2O_7$ an excellent host for rare earth-based phosphors and scintillators.

Eu^{3+} ion has been chosen as a dopant ion in this study owing to its narrow red emission, high color purity, symmetry sensitive red/orange emission, and so forth. Moreover, among the various methods explored to enhance the luminescence efficiency of bulk and powder phosphors,[25] Li^+ co-doping has been found to enhance their optical properties by modifying the local crystal field around the activator ions. With its small radius, Li^+ ions can be easily incorporated into the host lattice. However, to the best of our knowledge, there is no report on the luminescence properties of undoped YHO, Eu^{3+}-doped YHO (YHOE), and Eu, Li co-doped YHO for photo/radioluminescent phosphors, and in particular, no experiment reports on Li^+ doped YHO nanoparticles (NPs) and the corresponding luminescence enhancement.[26–28] Therefore, in this work, we have synthesized YHO NPs and red light emitting YHOE NPs using a molten salt synthesis (MSS) method. We have also demonstrated that the former has dual blue and red emission bands and the latter has high concentration quenching of 10% and a quantum efficiency of 12%. Intense radioluminescence from the YHOE NPs highlights their potential as X-ray scintillators. Co-doping with a Li^+ ion demonstrated a further improved emission output, quantum efficiency and excited state lifetime for the YHOE NPs.

To support our experimental results, we have performed density functional theory (DFT) based calculations to consider the different charge states of the oxygen vacancies (0, +1 and +2) by identifying their effects on the luminescence properties of YHO.[29–32] Moreover, oxygen defect formation energies were calculated to show the formation feasibility of these defects. The DFT studies confirmed the presence of neutral and ionized oxygen vacancies in the bandgap of the YHO NPs and the emission was correlated with these defect states. Furthermore, to explore the origin of the emission, structural stability, and the role of Li^+-co-doping theoretically, we have used DFT calculations to demonstrate that Li^+-co-doping increases the covalent character of the Eu^{3+}–O^{2-} bonding in the EuO_8 polyhedra.

Polymer nanocomposites provide a potential solution to meeting the technological requirements in view of the unique properties of NPs, with the processability, structural flexibility, and thermal, mechanical and optical properties of polymers, while simultaneously preventing the agglomeration of NPs.[33,34] Incorporation of YHOE NPs in a polymer system can significantly increase the physical parameter range beyond that of the host polymer and the NPs. In this work, we added the YHOE NPs into polyvinyl alcohol (PVA) and made nanophosphor-polymer thin films (NPTFs) which exhibit a high transparency and uniform red emission.

2. Experimental

The YHO, YHOE and Li-co-doped YHOE NPs were synthesized using an MSS method using KNO_3–$NaNO_3$ as the reaction medium at 650 °C.[35–38] The details of the synthesis method have been explained in the ESI as S1.† Moreover, the preparation of the NPTFs employing the YHOE NPs and PVA has also been discussed in detail in S1.†

The undoped sample is designated as YHO, whereas the doped samples with Eu^{3+} concentrations of 0.5, 1.0, 2.0, 5.0, 7.5, 10.0, 12.5, and 15.0% are designated as YHOE-0.5, YHOE-1.0, YHOE-2.0, YHOE-5.0, YHOE-7.5, YHOE-10.0, YHOE-12.5, and YHOE-15.0, respectively. Similarly, the Li^+ co-doped YHOE-0.5 NPs with Li^+ concentrations of 0.5, 1.0, 1.5, 2.0, 2.5 and 3.0% are designated as YHOE-0.5-Li0.5, YHOE-0.5-Li1.0, YHOE-0.5-Li1.5, YHOE-0.5-Li2.0, YHOE-0.5-Li2.5 and YHOE-0.5-Li3.0, respectively, and the 2.0% Li^+ co-doped YHOE NPs with Eu^{3+} concentrations of 0.5, 1.0, 2.0, 5.0, 7.5, 10.0, 12.5 and 15.0% are designated as YHOE-0.5-Li2.0, YHOE-1.0-Li2.0, YHOE-2.0-Li2.0, YHOE-5.0-Li2.0, YHOE-7.5-Li2.0, YHOE-10-Li2.0, YHOE-12.5-Li2.0 and YHOE-15.0-Li2.0 NPs, respectively.

The instrumental details of the various characterization techniques such as X-ray diffraction (XRD), field emission scanning electron microscopy (FESEM), Raman spectroscopy, energy dispersive spectroscopy (EDS), X-ray photoelectron spectroscopy (XPS), photoluminescence (PL), radioluminescence (RL) and time resolved emission spectroscopy (TRES) are described in the ESI as S2.† The theoretical methodology adopted in this work for the DFT calculations are mentioned in the ESI as S3.† The DFT calculated equilibrium volumes and bond-lengths found using GGA/LDA (generalized gradient approximation/local density approximation) and the bandgap, found using the HSE06 (Heyd–Scuseria–Ernzerhof) method are provided in Table S1 (ESI).†

3. Results and discussion

3.1. Materials characterizations: XRD, Raman and SEM

Both the XRD patterns (Fig. S1a†) and Raman spectra (Fig. S1b†) confirm the synthesized YHO and YHOE (0.5–15%)

NPs have a cubic fluorite structure. The EDS and XPS spectra were recorded on one of the representative samples, for example YHOE-5, and the corresponding data are shown in Fig. S1c and S1d,† respectively. The calculated crystal size of these NPs (Table S2†) is ∼30 nm, while the particle size estimated from the SEM images (Fig. S2†) ranges from 82 to 47 nm. The special quasi-random structure of YHO considered for the DFT simulations in the disordered fluorite structure is shown in Fig. S1e.† The blue, black and red spheres represent the Y, Hf and O atoms, respectively.

3.2. YHO NPs

3.2.1 PL properties. The emission spectrum of the YHO NPs (Fig. 1A) under excitation at 330 nm displays two bands in the ranges of 400–500 nm and 680–730 nm corresponding to bluish-green and deep red emissions, respectively. We could not find a significant difference with the 285 nm excitation except for a slight reduction in the emission intensity of both bands. This multicolor emission is typical in the presence of defect states in the band gap of materials, specifically oxygen vacancies (OVs), internal defects and self-trapped excitons (STEs).[39–42] OVs can be neutral, singly ionized and doubly ionized. In the YHO NPs, there are possibly two kinds of structural defects contributing to the PL emissions. Their origins could be different based on the different excitation spectra observed under emission wavelengths of 445 and 710 nm (Fig. S3a†).[43,44] The color coordinate calculated for the YHO NPs confirms the bluish-white emission (Fig. S3b and c†).

3.2.2 DFT calculations. To probe the exact electronic transitions involved in such emissions from the YHO NPs, we employed DFT based HSE06 simulations to calculate the electronic density of states (DOS) of ideal YHO and the change in the electronic DOS in the presence of neutral (V_{O^0}), +1 ($V_{O^{1+}}$) and +2 ($V_{O^{2+}}$) charged OVs. To generate a defect structure, an oxygen atom was removed from an 88 atom special quasirandom structure (SQS) supercell. The generated defect structures were thoroughly optimized with respect to volume (or lattice parameter) and atomic positions (ESI S3, Table S1†). Therefore, the defect concentration in our calculation was 1/88 or 1.136%.

The total and orbital angular momentum resolved DOS of YHO with the Fermi level set to 0 eV (Fig. 1B, i) shows that the electronic states below the Fermi level (or the valence band (VB)) are dominated by p–d bonding between the O 2p and Hf 5d states. The conduction band (CB) is mainly composed of the 4d states of Y and anti-bonding states of Hf 5d states. Our HSE06 calculated electronic bandgap of 3.98 eV demonstrates the insulating character of YHO. The total and angular momentum decomposed DOS owing to the presence of a neutral O vacancy (V_{O^0}) (Fig. 1B, ii) demonstrates that the overall nature of the VB remains unaltered, but an impurity band appears 3.4 eV ahead of the VB maximum in the

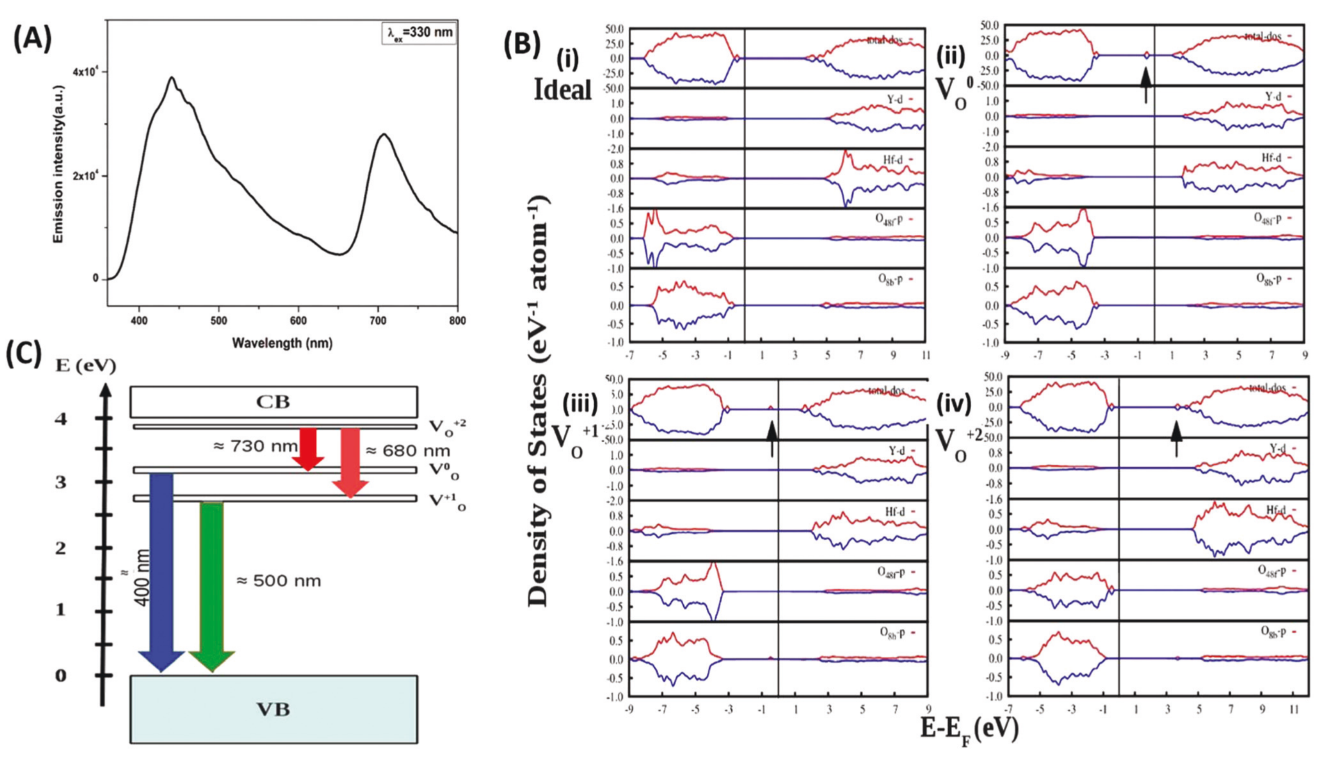

Fig. 1 (A) Emission spectrum (λ_{ex} = 330 nm) of the YHO NPs, (B) HSE06 calculated total and angular momentum decomposed DOS of: (i) ideal defect free YHO and YHO with (ii) a neutral oxygen vacancy (V_{O^0}), (iii) an oxygen vacancy of charge +1 ($V_{O^{1+}}$), and (iv) an oxygen vacancy of charge +2 ($V_{O^{2+}}$). Defect states are marked by an arrow in the bandgap. The vertical lines at 0 eV represent the Fermi energy. (C) Summary of the defect state distribution within the band gap of YHO.

bandgap and just below the Fermi level. This impurity state is doubly occupied and is mainly contributed to by the La-d/f states and O-p states. The total and angular momentum decomposed DOS owing to the presence of an O vacancy with a charge +1 ($V_{O^{1+}}$) (Fig. 1B, iii), which means that the V_{O^0} becomes $V_{O^{1+}}$ by trapping a hole from its surroundings. The overall nature of the VB remains unaltered, but singly occupied impurity states appear 3.0 eV ahead of the VB maxima. This impurity state is generated because the spin-up component is filled with electrons as it is situated below the Fermi energy. The impurity levels are composed of Hf-d states and O-p states. The total and angular momentum decomposed DOS owing to the presence of an O vacancy with a charge of +2 ($V_{O^{2+}}$) (Fig. 1B, iv) shows that the overall nature of the VB remains unaltered, but an impurity band appears below the CB minimum in the bandgap. The Fermi level is situated above the VB maximum. The impurity levels are composed of Hf-d states and O-p states in both the spin-up and spin-down components.

Based on our DFT-HSE06 calculations, we have summarized the location of the defect states in the band-gap region of YHO (Fig. 1C). The broad emission peak around 400–500 nm from the YHO NPs corresponds to an optical emission between the states situated 3.0–2.5 eV from each other, that is the optical emission between the defect states of V_{O^0} and $V_{O^{1+}}$ to VB (marked by the blue and green arrows). In YHO, the defect states close to 4.0 eV consist of $V_{O^{2+}}$. The broad emission peaks around the 680–730 nm region, which are situated 1.7–1.8 eV away from each other, originate from the transition between the $V_{O^{2+}}$ defect state → (V_{O^0}, $V_{O^{1+}}$) (marked by the red and deep red arrows). Therefore, our DFT-HSE06 results qualitatively provide an explanation for the origins of the broad emission peaks from the YHO NPs.

The DFT-GGA calculated oxygen defect formation energies in the dilute limit for neutral (V_{O^0}) and charged ($V_{O^{1+}}$ and $V_{O^{2+}}$) oxygen defects (Fig. S3c†) indicate that the formation of $V_{O^{2+}}$ defects is most favored close to the VB compared to those of the $V_{O^{1+}}$ and neutral oxygen defects and that the oxygen vacancies have a tendency to donate electrons.[45] The formation of a neutral oxygen vacancy is energetically less favorable compared to that of the charged oxygen defects. The vacancy formation energies of the 1+ and 2+ oxygen defects become close with a difference of 0.5 eV at the Fermi level. With the increasing Fermi energy, the vacancy formation energy of the $V_{O^{1+}}$ defect becomes most favorable compared to those of the V_{O^0} and $V_{O^{2+}}$ defects. As the vacancy formation energies of the V_{O^0}, $V_{O^{1+}}$ and $V_{O^{2+}}$ defects become closer, the oxygen defects are expected to strongly participate in the PL emission from the YHO NPs.

3.3. YHOE NPs

3.3.1 Excitation PL spectra. In the PL excitation spectra (Fig. 2a), the broad band in the range of 240–310 nm can be attributed to the O^{2-} → Eu^{3+} charge transfer (CT) transition corresponding to the electron transfer from the filled 2p shell of the O^{2-} ions to the empty 4f shell of the Eu^{3+} ions. There is no regular trend for the energy of the CT band or its full width half maximum (FWHM) as a function of the Eu^{3+} concentration. The sharp peaks in the range of 350–550 nm are related to the interconfigurational (Xe)4f^6 → (Xe)4f^6 transitions of the Eu^{3+} ions. The most attractive features of the excitation spectra are the highly intense near UV (393 nm) and blue (465 nm) bands due to the $^7F_0 \rightarrow {}^5L_6$ and $^7F_0 \rightarrow {}^5D_2$ transitions, which indicate that the YHOE NPs can serve as color converters for LED applications because of their high spectral overlap cross section with an emission spectra for efficient LEDs.

3.3.2 Emission PL spectra. The YHOE NPs show bright red luminescence when excited with a UV lamp (Fig. 2b) with characteristic Eu^{3+} spectral features of $^5D_0 \rightarrow {}^7F_J$ transitions (J = 1–4). Specifically, the emission peaks at 592, 612, 653, and 710 nm are from the $^5D_0 \rightarrow {}^7F_1$, $^5D_0 \rightarrow {}^7F_2$, $^5D_0 \rightarrow {}^7F_3$ and $^5D_0 \rightarrow {}^7F_4$ transitions, respectively. Among them, the 592 nm peak is the magnetic dipole $^5D_0 \rightarrow {}^7F_1$ transition (MDT) which is independent of the chemical environment surrounding the Eu^{3+} ions. The most intense band at 612 nm is ascribed to the hypersensitive electric dipole $^5D_0 \rightarrow {}^7F_2$ transition (EDT), which is normally observed when the Eu^{3+} ions are localized at sites without a center of inversion (C_i). The YHOE NPs have a highly disordered fluorite structure as confirmed by XRD and Raman spectroscopy (Fig. S1†). Therefore, most Eu^{3+} ions are localized in a highly disordered fluorite structure which lacks inversion symmetry. Consequently, the highly intense red emissions from the electric dipole transitions of $^5D_0 \rightarrow {}^7F_2$ and $^5D_0 \rightarrow {}^7F_4$ are observed and the intensity of the EDT peak is higher than that of the MDT peak. Based on these concentration dependent emission profiles, the dominance of the EDT over the MDT at all Eu^{3+} doping concentrations indicates the majority of Eu^{3+} ions have an asymmetric local surrounding. Fig. S4a, b and c† shows the HSE06 calculated DOS of Eu^{3+} doped YHO (in Y^{3+} site) in a system containing V_{O^0}, $V_{O^{1+}}$ and $V_{O^{2+}}$, respectively. The overall DOS is similar to their V_{O^0}, $V_{O^{1+}}$ and $V_{O^{2+}}$ counterparts. The Eu^{3+} doping at the Y^{3+} site lifts the degeneracy in the defect states and generates shallow defect states close to the CB minima. The Eu-d states are present throughout the VB and CB energy region of YHO and good matching in the distribution of the Eu-d states can be found with the VB/CB energy region of the YHO. This allows for a good energy transfer efficiency from the host to the Eu^{3+} ion.

The PL emission intensity of the YHOE NPs is strongly governed by the dopant concentration (Fig. 2c). The integral emission intensity (φ) from 600 to 640 nm corresponding to the $^5D_0 \rightarrow {}^7F_2$ transition progressively increases as the Eu^{3+} doping concentration increases from 0.5 to 10.0 mol% (Fig. 2c). For Eu^{3+} doping concentrations higher than 10.0%, the corresponding φ decreases, which is attributed to the concentration quenching phenomenon. Therefore, the critical quenching concentration of our YHOE NPs is 10.0%, which is high enough to produce efficient nanophosphors.

For dopant-based phosphors, the critical quenching concentration strongly depends on the solubility of the dopant ions in the host matrix which depends on the selection of the dopant and host. In most phosphors, low solid solubility of dopant ions leads to their segregation in the host lattice,

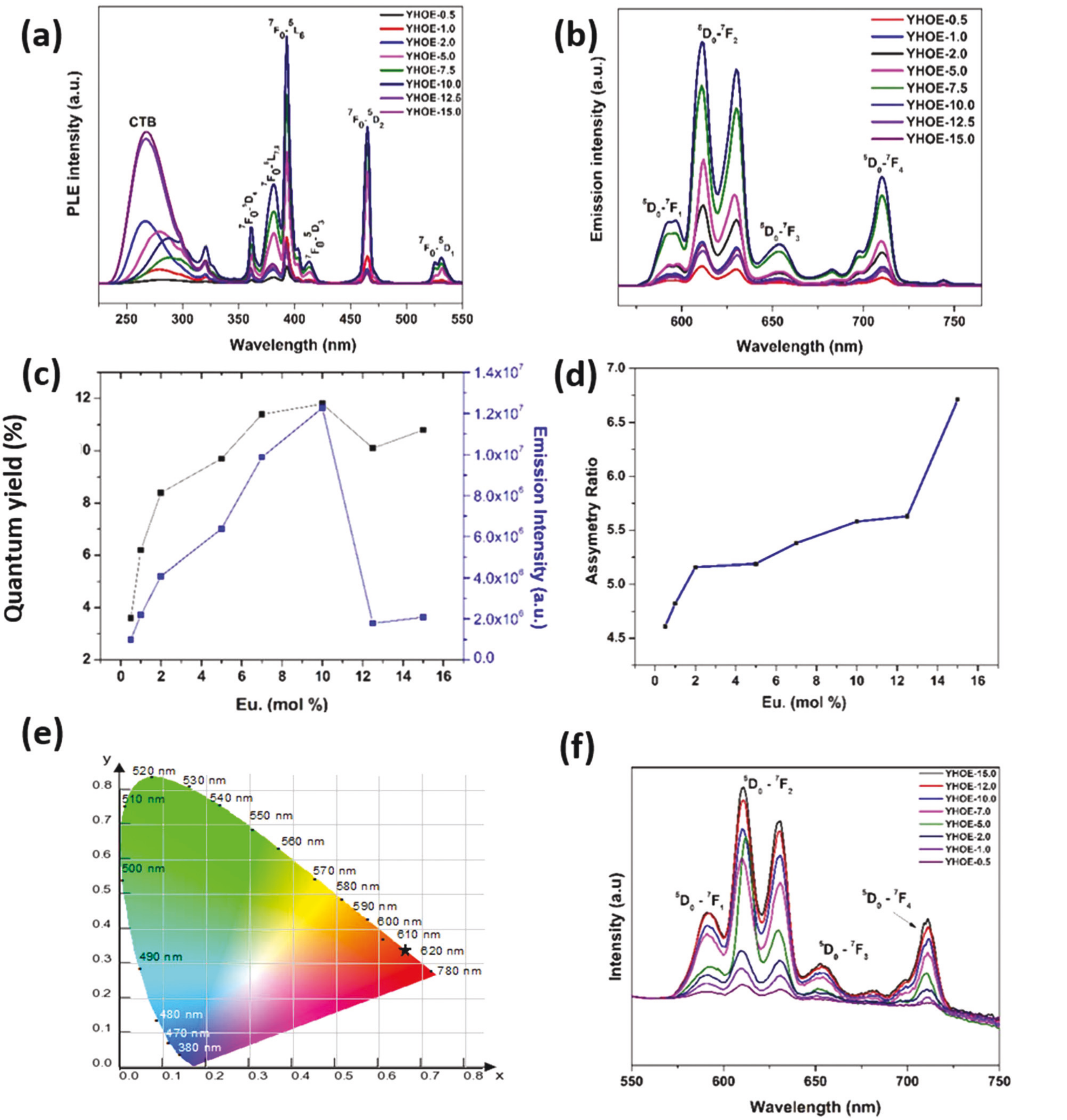

Fig. 2 (a) PL excitation spectra (λ_{em} = 612 nm), (b) PL emission spectra (λ_{ex} = 393 nm), (c) quantum yield and integrated PL emission intensity of the $^5D_0 \rightarrow {}^7F_2$ transition (λ_{ex} = 393 nm) as a function of the Eu^{3+} doping concentration, (d) asymmetry ratio, (e) chromaticity diagram (of the YHOE-10.0 NPs), and (f) RL spectra of the YHOE NPs.

which results in concentration quenching at low doping concentrations. As listed in Table S3,† when the trivalent Eu^{3+} dopant occupies divalent and/or tetravalent sites, charge compensating defects lead to high strain which limits the quenching concentration to low values. Concentration quenching occurs when the excitation energy (E_{exc}) migrates and reaches the quenching center, in which E_{exc} is lost nonradiatively rather than being converted into the radiative emission of a photon. High concentration quenching relies on the intrinsic crystal structure of the hosts and large nanocrystals can accommodate more active doping ions compared to bulk materials. Moreover, high concentration quenching of the YHOE NPs indicates trivalent europium ions with a red emission. For our YHOE NPs, Eu^{3+} and Y^{3+} ions have the same ionic charge and similar ionic size, which results in a high solid solubility and uniform dispersion of Eu^{3+} ions in the YHO matrix, even at high doping concentrations. The nanocrystalline nature of the synthesized YHOE NPs also helps to achieve the high quenching concentration. Improvements in the quenching concentrations were also observed when going from the bulk to nano in other RE doped nanophosphors as well.[46,47] This is attributed to the low density of the traps in the nanosystems owing to the limited primitive cells per particle.[47] Also the doping uniformity in nanomaterials minimizes the segregation of ions and prevents local concentration quenching.[48]

One can calculate the minimum distance between the dopant ions and quenching centers which facilitates non-radiative energy transfer and leads to a decrease of the emission intensity using an empirical relation given by Blasse:[49]

$$r_c = 2\left(\frac{3V}{4\pi X_c N}\right)^{\frac{1}{3}} \tag{1}$$

In which r_c is the critical distance between the dopant ion and quenching center, V is the volume of the unit cell of the host matrix, X_c is the critical concentration of the dopant ions after which concentration quenching takes place, and N is the number of cations per unit cell of the host lattice. For a YHO host lattice, V = 145.83 Å^3, N = 32 (four formula units per unit cell), and X_c = 0.1, therefore the calculated critical distance is 4.43 Å. In other words, the Eu^{3+}–Eu^{3+} distance in the YHOE NPs is smaller than 10 Å. Therefore, for the concentration quenching of our YHOE NPs, exchange interaction is the main mode of non-radiative energy transfer among the Eu^{3+} ions in the YHO host.

3.3.3 Asymmetry ratio. The integral intensity ratio of the EDT ($^5D_0 \rightarrow {}^7F_2$) and MDT ($^5D_0 \rightarrow {}^7F_1$) peaks, known as the asymmetry ratio (R_{21}), defines the structural distortion around the Eu^{3+} ions in the host lattice. The R_{21} of the YHOE NPs increases with increasing Eu^{3+} dopant concentration progressively (Fig. 4d). This trend suggests a more favorable asymmetric environment of Eu^{3+} ion in the YHO lattice with the increasing doping level, which indicates a more disordered YHO matrix lattice at a higher doping concentration. Therefore, the electric dipole induced emission ($^5D_0$–$^7F_2$) is the most intense peak from the YHOE NPs under near UV excitation. Correspondingly, the asymmetry ratio of the YHOE-15.0 NPs is the highest, which is close to 7. Based on Table S4,† the YHOE NPs display the highest asymmetry ratio compared to the reported Eu^{3+} doped pyrochlore phosphors, which suggests that they have a high red color purity for achieving a desirable performance in phosphor driven white LEDs.

3.3.4 Quantum yield. As an important parameter for commercial and practical purposes, the quantum yield (QY) values of the YHOE NPs were measured and calculated using the following equation:[50]

$$\mathrm{QY} = \frac{\int F_S}{\int L_R + \int L_S} \tag{2}$$

where F_S represents the emission spectrum of a sample, L_R is the spectrum of the excitation light from the empty integrated sphere (without sample), and L_S indicates the excitation spectrum of the excited sample. The experiments were performed in a similar way to our previous publications.[51] The QY value of the YHOE NPs increases from 3.5% to 12% as the Eu^{3+} doping concentration increases from 0.5% to 10.0% and then slightly reduces (Fig. 2c). The latter is again attributed to the non-radiative energy transfer among the Eu^{3+} ions at a high doping concentration causing concentration quenching. Among several reported Eu^{3+} doped pyrochlore phosphors, the QY of the YHOE NPs is good (Table S5†).

3.3.5 Colorimetric performance. As there is no obvious spectral profile change for the YHOE NPs as a function of the Eu^{3+} doping concentration, the Commission Internationale de l'Eclairage (CIE) chromaticity coordinates were evaluated for the YHOE-10.0 NPs. The corresponding CIE index diagram shows that the YHOE NPs emit intense red light with CIE coordinates of 0.665 and 0.343 (Fig. 2e), which are in close agreement with the international standard chromaticity coordinates of the commercial red phosphors: $Y_2O_2S:Eu^{3+}$ (x = 0.642 and y = 0.341) and $Y_2O_3:Eu^{3+}$ (x = 0.650 and y = 0.356).[30,35,36,44,52]

3.3.6 Lifetime spectra. All of the YHOE NPs exhibit biexponential decay under 393 nm excitation and 612 nm emission wavelengths (Fig. S5a†) and can be fitted using the equation:

$$I(t) = A_1 \exp(-t/\tau_1) + A_2 \exp(-t/\tau_2) \tag{3}$$

In which $I(t)$ is the PL emission intensity at time t, A_1 & A_2 are residual weighting factor of each lifetime, t is the time of measurements, and τ_1 and τ_2 are the lifetime values of the first and the second components, respectively. The biexponential PL decay behavior can be caused by different amounts of energy transfer and nonradiative decay of dopant ions localized near the surface and the core of the NPs and the non-uniform distribution of dopant ions in the host matrix.[53] For our defect fluorite structured YHOE NPs, there are two cation polyhedra: an ideal cube-like YO_8 and a highly distorted HfO_6. Usually the long lifetime component (τ_2) is attributed to the lanthanide dopants located at the symmetric environment as f–f transitions are forbidden by the La-Porte selection rule.[54,55] On the other hand, the short lifetime component (τ_1) is assigned to the lanthanide dopants localized in the asymmetric environment. In our case, the τ_2 component (2.0–2.6 ms) is attributed to the Eu^{3+} ions occupying the highly symmetric YO_8 cube owing to the closeness of the ionic radii and the matching trivalent charge of the Eu^{3+} and Y^{3+}. The τ_1 component (0.56–1.05 ms) is attributed to the Eu^{3+} ions occupying the distorted HfO_6 octahedra.

The average lifetime value of the YHOE NPs increases from 1.78 to 2.02 ms with the increasing Eu^{3+} doping concentration from 0.5% to 10% and then decreases with a further increase of Eu^{3+} (Table S6 and Fig. S5b†), similar to the observed trends in their PL intensity and QY (Fig. 2c). Moreover, the fraction of the long-lived species situated at the Y^{3+} site is much higher than the short-lived species localized at the Hf^{4+} site (Table S6†).[30,35,36,38,44,56,57] The lifetime values for our YHOE NPs are similar to those reported for other Eu^{3+} doped pyrochlore phosphors (Table S7†).

3.3.7. Structural stability of Eu^{3+} dopant ions in the YHO host. To understand the structural stability of the Eu^{3+} dopant ions in the YHO host, the cohesive energies of the Eu^{3+}-doped YHO were calculated for Eu^{3+} doping at the Y^{3+} site and Hf^{4+} sites separately using DFT based calculations. These DFT based calculations have been used to predict the structural stability of the dopant ions in other $A_2M_2O_7$ compositions, particularly for hafnate and zirconate based systems.[30,35,36,44] This is done by calculating the cohesive energy of Eu^{3+} at the A^{3+} and M^{4+} sites. The one with the minimum cohesive energy has a higher structural stability and *vice versa*.[30,35,44] In our DFT calculations, a doping level for the Eu^{3+} ions of 1/88 (1.136%) in YHO was considered and full structural relaxations were performed. The Eu–O bond distances when Eu^{3+} was doped at the Y^{3+}/Hf^{4+} sites are shown in Table 1. From this table it can be clearly seen that the distribution of the Eu–O bond lengths is smaller when the Eu^{3+} is doped at the Y^{3+} site compared to the Hf^{4+} site, which signifies that the Eu^{3+} substitution is favorable at the Y^{3+} site considering the same charge state and closeness in ionic sizes. Therefore, from these DFT calculations we can conclude that the Y^{3+} site is energetically more favorable compared to the Hf^{4+} site implying the preferential occupation of the Eu^{3+} ions at the Y^{3+} site.

Moreover, our DFT calculation results are in agreement with the experimentally measured lifetime values, which shows that the fraction of the long-lived species occupying the Y^{3+} site is much greater than that of the short-lived species occupying the Hf^{4+} site.

3.3.8 Radioluminescence. When ionizing radiation is absorbed by a sample, electron–hole pairs are created following a typical scintillation mechanism. The emitted light is intense if the band gap between the excited state and the highest component of the ground state multiplet is large. RL light is generated when the host absorbs X-ray photons and electrons are promoted to the excitation level $^5D_0$ of Eu^{3+}, wherein they become activated. This is followed by the recombination of the activated electrons and holes, which finally transfer and recombine energy to the emitting centers (Eu^{3+} ions in this case). The room temperature RL emission spectra of the YHOE NPs (Fig. 2f) show similar profiles to their PL spectra. Both types of spectra exhibit bands centered at 592 nm ($^5D_0 \rightarrow {}^7F_1$), 613 nm ($^5D_0 \rightarrow {}^7F_2$), 653 nm ($^5D_0 \rightarrow {}^7F_3$) and 702 nm ($^5D_0 \rightarrow {}^7F_4$) of Eu^{3+} ions. Moreover, the intensity of the hypersensitive EDT peak is much higher than that of the MDT peak under X-ray excitation too, which indicate that the majority of Eu^{3+} ions are localized in a highly asymmetric environment lacking a center of symmetry. This confirms that X-ray irradiation can generate a similar emission spectrum as UV light. However, the RL emission intensity is lower than the PL emission intensity, which could be due to the lower power density of the applied X-ray under normal conditions compared to that of the UV excitation source (5 mW cm^{-2}). Unlike the observed PL concentration quenching at the 10% Eu^{3+} doping level, in the case of PL, no RL quenching was observed from our YHOE NPs with the highest Eu^{3+} doping level of 15% in this study. For efficient scintillators, host materials containing heavy elements are crucial for the photoelectric absorption of X-rays. With the heavy element constituent of Hf (Z = 72) and the intrinsic defect emission, YHO serves as an efficient X-ray antenna by absorbing X-ray photons and transferring them to Eu^{3+} activators. Thus, our YHOE NPs exhibits highly efficient X-ray excited luminescence compared to the other scintillators without a heavy atomic component. The mechanism of the X-ray excited luminescence in the YHOE NPs is explained in the ESI, file S7,† along with schematic diagram shown in Fig. S6.†

Table 1 DFT calculated Eu–O bond distances when Eu^{3+} is doped at the Y^{3+}/Hf^{4+} site in YHOE NPs

	Eu–O bond distances							
Eu doped at Hf^{4+} site	2.29	2.29	2.41	2.41	2.43	2.44	2.60	2.72
Eu doped at Y^{3+} site	2.30	2.35	2.35	2.40	2.44	2.50	2.51	2.56

3.4. Li Co-doped YHOE NPs

3.4.1 Luminescence spectroscopy studies. To study the co-doping effect of Li^+ on the luminescence performance of the YHOE NPs, we first kept the Eu^{3+} concentration at 0.5% and varied the Li^+ concentration between 0 and 3.0%. From the PL emission spectra of the Li^+ co-doped YHOE-0.5 NPs (Fig. 3a), the optimal co-doping concentration of Li^+ with a maximum PL emission output is 2.0%, this is mainly due to the enhanced radiative transition rate from the Li^+ co-doping.[58] The excitation spectra from the same series of samples also show similar trends (Fig. S7a†). There are several factors responsible for the PL enhancement of the Li^+ co-doping of phosphors, including modification of the symmetry of the primary dopant ions, reduced defects, charge compensation and the introduction of OVs into the host crystals.[59] After the optimum Li^+ co-doping concentration of 2.0%, the created oxygen vacancies and other defects cause suppression of the PL emission output by providing non-radiative pathways.[60]

With the optimum Li^+ co-doping concentration of 2.0%, the quenching concentration was found to be 12.5% of Eu^{3+} ions in the YHO host NPs (Fig. 3b), a 2.5% increase from the YHOE NPs without Li^+ co-doping (Fig. 2c). It is believed that this increase provides better control over the defects by means of Li^+ co-doping.[61] Similarly, the PL excitation spectra of the Li^+ co-doped YHOE NPs show similar trends (Fig. S7b†).

Fig. 3c compares the PL excitation spectra of the YHOE-12.5 NPs before and after 2.0% Li^+ co-doping. There are some interesting features observed after Li^+ co-doping. First, the Charge Transfer Band (CTB) energy becomes lower after co-doping, whereas the reverse is true for the f–f transitions at 395 and 465 nm. The former can be attributed to a reduction in the ionic character of the YHO host in the presence of the highly electropositive Li^+ ion. The Li^+ co-doping may also enhance the covalency of the Eu^{3+}–O^{2-} bond and the coordination environment of the Eu^{3+} ion site to reduce the charge transfer energy.[52] Overall, Li^+ co-doping improves the absorption of the

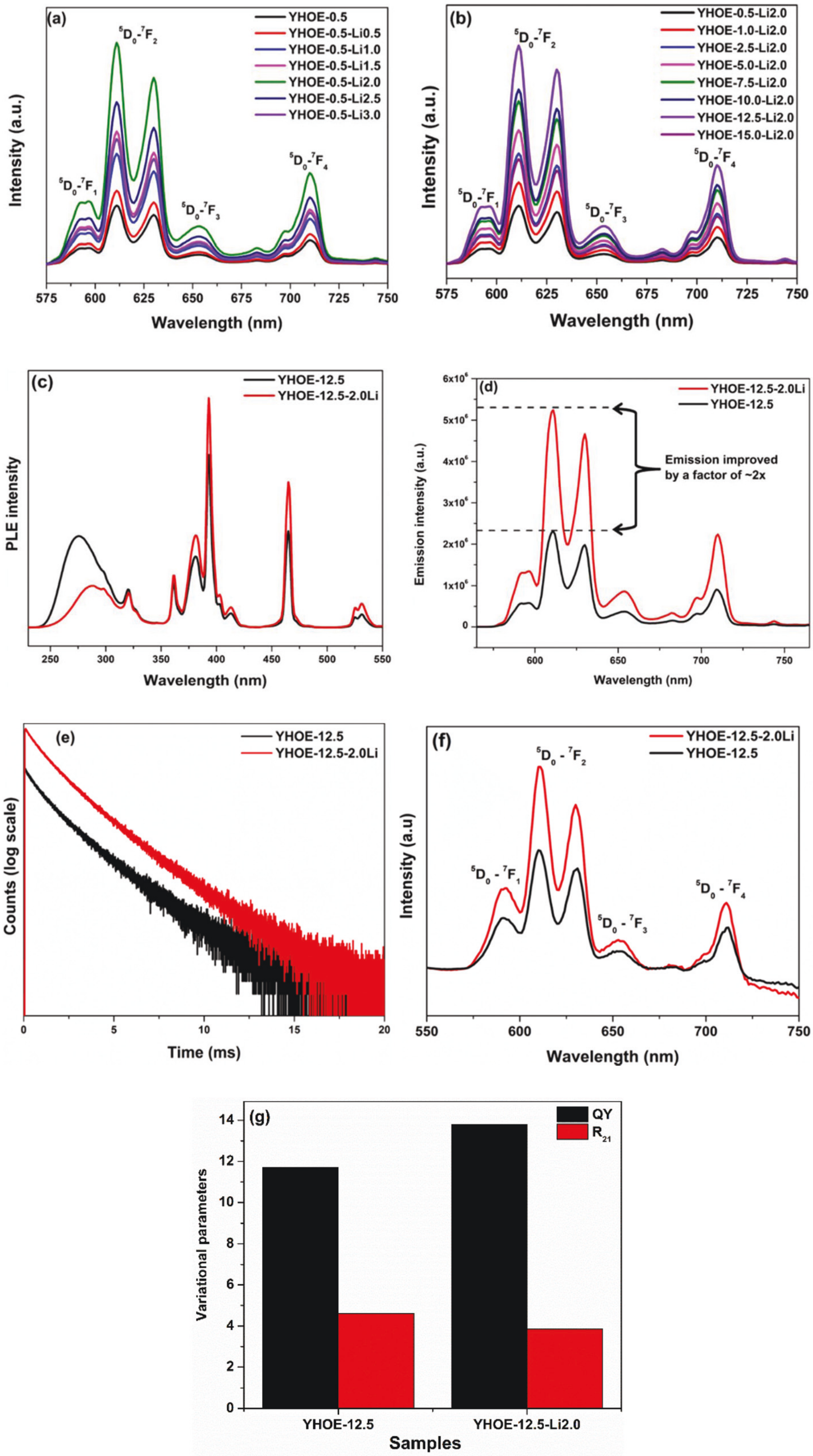

Fig. 3 (a) PL emission spectra of the YHOE-0.5 NPs with different Li^+ co-doping concentrations. (b) PL emission spectra of the YHOE NPs with a 2.0% Li^+ co-doping concentration with various Eu^{3+} concentrations. Comparison of the YHOE-12.5 NPs before and after 2.0% Li^+ co-doping: (c) excitation spectra, (d) emission spectra, (e) luminescence decay profiles, (f) RL spectra, and (g) QY and asymmetry ratio.

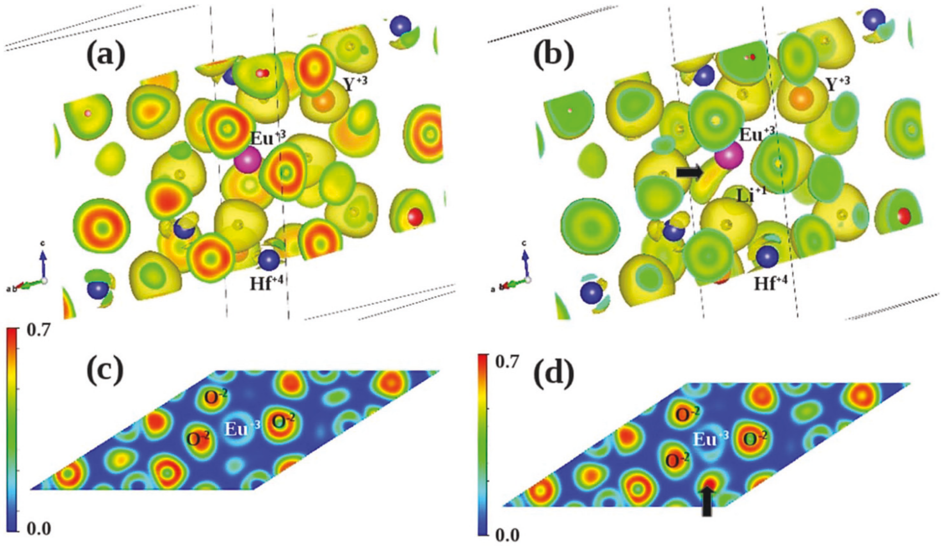

Fig. 4 Electron localization function (ELF) plots of (a) Eu^{3+} substituted in a YO_8 polyhedra and (b) Li co-doped (in an O^{2-} site) and Eu^{3+} substituted in a YO_8 polyhedra (Eu in pink, Y in red, Hf in blue, O in black, and Li atom in green). The 2-dimensional charge density distribution (in e $Å^{-3}$) plots in the (002) plane for (c) the Eu^{3+} substituted and (d) Li co-doped and Eu^{3+} substituted cases.

YHOE NPs in the region of 350–550 nm, which is important for their commercial applications from the perspective of near UV and blue light excitations.

From the PL emission spectra of the YHOE-12.5 NPs before and after 2.0% Li^+ co-doping, we can see that the emission intensity doubles (Fig. 3d). A similar enhancement in the PL emission has been reported from a few Eu^{3+} doped phosphors in the literature, although quantification of the extent of enhancement is lacking.[58–60] There is an enhancement in the decay lifetime of the YHOE NPs from 2.02 to 2.43 ms upon Li^+ co-doping (Fig. 3e). Li^+ co-doping has also been explored to enhance the emission output of the lanthanide doped phosphors using non-optical excitation processes such as cathodoluminescence or X-ray excitation.[62] Upon Li^+ co-doping, the RL intensity of the YHOE-12.5 NPs is enhanced (Fig. 3f). A similar RL intensity enhancement was also obtained from Y_2O_3:Eu NPs upon Li^+ co-doping.[63] These observations correlate with the decrease of the asymmetry ratio R_{21} (from 4.62 to 3.85) and the increase of the QY (from 12 to 13.6%) (Fig. 3g). Small ions, such as Li^+, can readily enter the interstitial sites of the YHO host to reduce the crystal field symmetry around the Eu^{3+} ions. Lattice altercation is induced by the formation of Eu⋯O⋯Li types of moiety, wherein the local surrounding of the Eu^{3+} ions becomes modified owing to the redistribution of the electron density around the oxygen ions, therefore more electrons are pulled toward the Eu^{3+} ions.[64] Moreover, incorporation of the Li^+ ions at the Y^{3+} site leads to the generation of oxygen vacancies through the following reaction:

$$Li^{\bullet} + 2Y_Y^{\bullet\bullet\bullet} \leftrightarrow 2Li_Y'' + O_o^x + V_O^{\bullet\bullet} \quad (4)$$

The $V_O^{\bullet\bullet}$ defects act as the sensitizer for the Eu^{3+} ions and cause a very efficient radiative energy transfer to Eu^{3+} ions owing to the strong mixing of CTB, thus leading to an increase in the emission intensity.[65] After Li^+ co-doping, the reduced R_{21} of the YHOE-12.5 NPs indicates a more symmetrical environment around the Eu^{3+} ions for a longer decay lifetime. This aspect is highly useful in exploring NPs for fluoroimmunoassays. Moreover, Li^+ incorporation improves the crystallinity of the phosphor host,[62] reduces the surface defects, enhances the phonon–electron interaction, reduces the internal reflections and decreases the non-radiative transitions,[66,67] thus the improvement in the emission intensity.[68,69]

3.4.2 DFT studies on the role of Li^+ co-doping. To further understand the effects of Li co-doping on the YHOE NPs, two separate DFT calculations were performed. In one calculation, a single Eu^{3+} ion substituted an Y^{3+} site of an 88-atom SQS cell to form the EuO_8 polyhedra. In another calculation, a single Li atom was substituted in the EuO_8 polyhedra in place of an oxygen atom. These two 88 atom SQS cells were optimized with respect to the volume and atomic positions. Fig. 4a and c clearly show that the electron clouds are distributed around the O atoms non-spherically, indicating the Eu^{3+}–O^{2-} bonding has an ionic and covalent character. Upon Li^+ co-doping, an additional electron cloud appears in the Li^+ co-doped EuO_8 polyhedra marked by the black arrow (Fig. 4b and d). As a result, after Li^+ co-doping, an almost spherical charge distribution around the Eu^{3+} ion becomes distorted and elongated, which implies an increase in the covalent character of the Eu^{3+}–O^{2-} bonding (Fig. 4c *vs.* d). This phenomenon agrees with our PL excitation spectral data which suggested a reduction in the CTB energy upon Li^+ co-doping owing to the increasing covalent character of the Eu^{3+}–O^{2-} bond. Fig. S8† shows the HSE06 calculated DOS of the Eu^{3+} doped and Li co-doped YHO (in a Y^{3+} site) in a system containing V_{O^0}, $V_{O^{1+}}$ and $V_{O^{2+}}$, respectively. Li co-doping generates shallow defect states close to the CB minima and the Li-p states contribute at the defect states in all oxygen vacancy types. Therefore, it is expected that the Li co-doping with Eu^{3+} doping will influence the defect related emission in the YHO and may improve the emission intensity and quantum efficiency.

3.5 Nanophosphor-polymer thin films

The excitation spectrum of the NPTFs under 612 nm emission (Fig. 5a) displayed similar features to that of the YHOE NPs. There is a broad peak around 259 nm corresponding to $O^{2-} \rightarrow Eu^{3+}$ CT along the f–f bands in the range of 350–550 nm similar to those of the YHOE NPs. On the other hand, the emission spectra (Fig. 5b) shows a typical Eu^{3+} profile under 259 and 393 nm excitations. The peak positions of the $^5D_0 \rightarrow {}^7F_2$ and $^5D_0 \rightarrow {}^7F_1$ transitions are unaltered after the YHOE NPs are dispersed in a PVA matrix. The relative excitation and emission intensities of the NPTFs are lower than those of the YHOE NPs because of the presence of a reduced number of Eu^{3+} ions per unit volume. In addition, the NPTFs are highly transparent (Fig. 5c) allowing various potential applications in the development of optoelectronic devices. A uniform red emission is also observed from the NPTFs (Fig. 5d) confirming the homogeneous distribution of the YHOE NPs in the PVA matrix. The luminescence decay profile (Fig. 5e) displays monoexponential behavior with a lifetime value of 1.73 ms. This is different from the YHOE NPs themselves which dis-

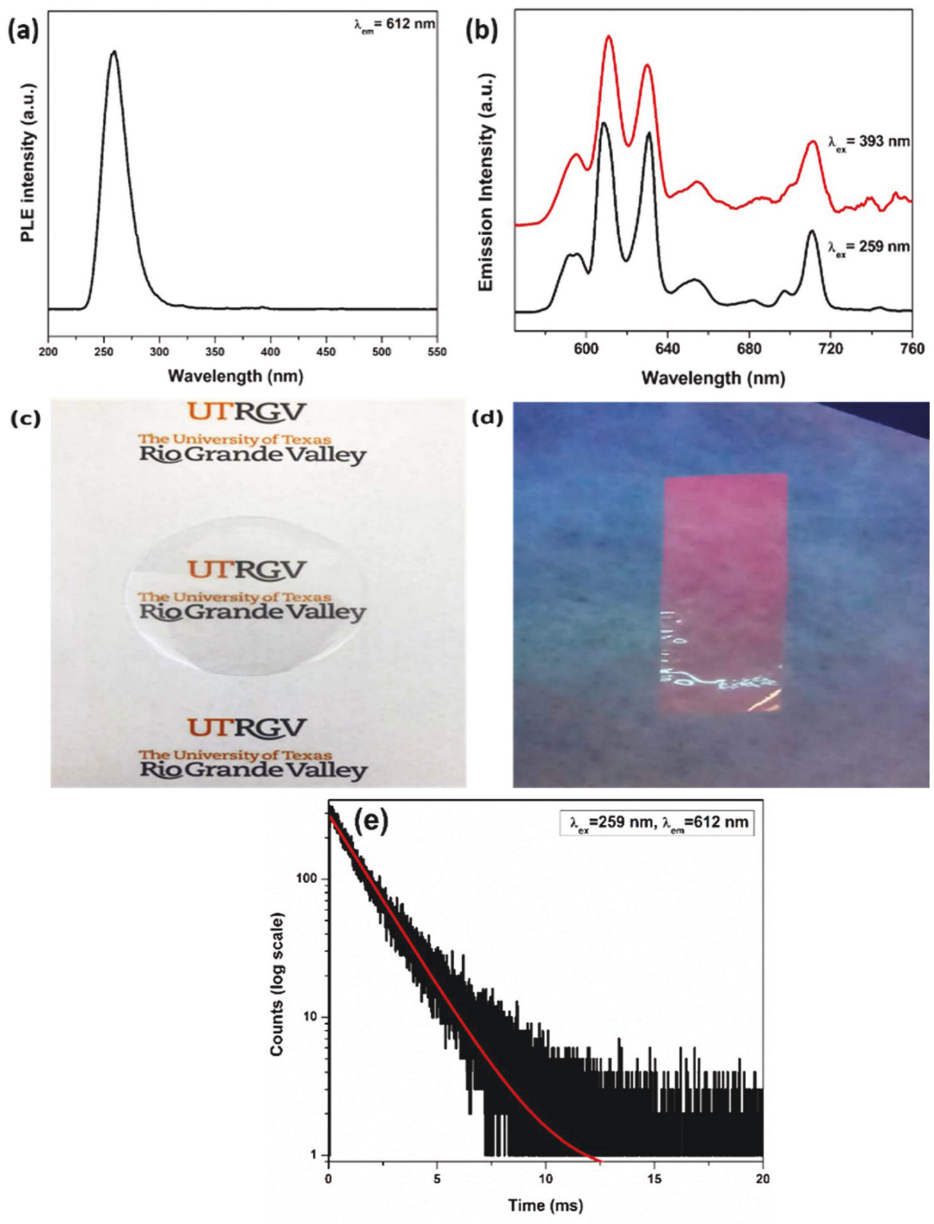

Fig. 5 The YHOE NPs-containing NPTFs: (a) excitation spectrum, (b) emission spectra (λ_{ex} = 259 and 393 nm), (c) photograph, (d) corresponding red emission under near UV excitation, and (e) luminescence decay profile.

played biexponential decay. This can be ascribed to the more homogenous environment offered by dispersing the YHOE NPs in the polymeric PVA matrix.

4. Conclusions

In this work, YHO, YHOE (Eu^{3+} = 0.5–15%) and Li^{+}-co-doped YHOE NPs were synthesized at 650 °C using molten salt synthesis. The undoped YHO NPs displayed violet and blue emissions under 330 nm excitation, which have been attributed of the presence of ionized oxygen vacancies in the bandgap based on DFT calculations. Eu^{3+} doping leads to an intense red emission at 612 nm, a long luminescence decay time and high concentration quenching. As Eu^{3+} and Y^{3+} have the same ionic charge and a similar ionic size, Eu^{3+} ions exhibit high solubility in the YHO host. The higher affinity of Eu^{3+} for Y^{3+} is also justified using the DFT calculated cohesive energy at both the Y^{3+} and Hf^{4+} site. This results in the uniform dispersion of the Eu^{3+} ions in the YHO matrix, even at high doping concentrations. Co-Doping Li^{+} ions in the YHOE lattice enhances the quantum efficiency and the excited state lifetime of the YHOE NPs. The DFT results show that Li^{+} co-doping increases the covalent character of the Eu^{3+}–O^{2-} bonding in the EuO_8 polyhedra. Our Li^{+}-co-doped YHOE NPs display optimum PL and RL output, which highlights their application potentials in solid state lighting and X-ray phosphors. In summary, our work demonstrates a highly efficient material for optoelectronics and scintillator applications with high concentration quenching, high color purity and a long lifetime. The YHOE NPs were also explored for making NPTFs which exhibited good emission properties, high transparency and a uniform red emission. They have potential applications in life sciences and optoelectronics.

Conflicts of interest

The authors declare no competing financial interests.

Acknowledgements

YM acknowledges financial support from the National Science Foundation under CHE (award #1710160) and the IIT startup funds. SKG thanks the United States-India Education Foundation (USIEF) and the Institute of International Education (IIE) for his Fulbright Nehru Postdoctoral Fellowship (award# 2268/FNPDR/2017). We also thank Dr J. Liu for technical support in the preparation of the YHOE-PVA nanocomposite thin films.

Notes and references

1 C. Jiang, M. Peng, A. M. Srivastava, L. Li and M. G. Brik, Mn^{4+}-Doped Heterodialkaline Fluorogermanate Red Phosphor with High Quantum Yield and Spectral Luminous Efficacy for Warm-White-Light-Emitting Device Application, *Inorg. Chem.*, 2018, **57**, 14705–14714.

2 Z. Zhang, C. Ma, R. Gautier, M. S. Molokeev, Q. Liu and Z. Xia, Structural Confinement toward Giant Enhancement of Red Emission in Mn^{2+}-Based Phosphors, *Adv. Funct. Mater.*, 2018, **28**, 1804150.

3 Y. Wang, J. Ding, Z. Zhao and Y. Wang, A Cerium Doped Scandate Broad Orange-Red Emission Phosphor and its Energy Transfer-Dependent Concentration and Thermal Quenching Character, *Inorg. Chem.*, 2018, **57**(23), 14542–14553.

4 W. Lü, Y. Jia, Q. Zhao, W. Lv and H. You, Design of a luminescence pattern via altering the crystal structure and doping ions to create warm white LEDs, *Chem. Commun.*, 2014, **50**, 2635–2637.

5 W. Lv, Y. Jia, Q. Zhao, M. Jiao, B. Shao, W. Lü and H. You, Crystal Structure and Luminescence Properties of $Ca_8Mg_3Al_2Si_7O_{28}$:Eu^{2+} for WLEDs, *Adv. Opt. Mater.*, 2014, **2**, 183–188.

6 C. Hecht, F. Stadler, P. J. Schmidt, J. S. auf der Günne, V. Baumann and W. Schnick, $SrAlSi_4N_7$:Eu^{2+}–A Nitridoalumosilicate Phosphor for Warm White Light (pc) LEDs with Edge-Sharing Tetrahedra, *Chem. Mater.*, 2009, **21**, 1595–1601.

7 H. Masai, G. Okada, A. Torimoto, T. Usui, N. Kawaguchi and T. Yanagida, X-ray-induced Scintillation Governed by Energy Transfer Process in Glasses, *Sci. Rep.*, 2018, **8**, 623.

8 H. Chen, A. L. Patrick, Z. Yang, D. G. VanDerveer and J. N. Anker, High-Resolution Chemical Imaging through Tissue with an X-ray Scintillator Sensor, *Anal. Chem.*, 2011, **83**, 5045–5049.

9 A.-L. Bulin, C. Truillet, R. Chouikrat, F. Lux, C. Frochot, D. Amans, G. Ledoux, O. Tillement, P. Perriat, M. Barberi-Heyob and C. Dujardin, X-ray-Induced Singlet Oxygen Activation with Nanoscintillator-Coupled Porphyrins, *J. Phys. Chem. C*, 2013, **117**, 21583–21589.

10 A. Kamkaew, F. Chen, Y. Zhan, R. L. Majewski and W. Cai, Scintillating Nanoparticles as Energy Mediators for Enhanced Photodynamic Therapy, *ACS Nano*, 2016, **10**, 3918–3935.

11 T. Guo, Y. Lin, W.-J. Zhang, J.-S. Hong, R.-H. Lin, X.-P. Wu, J. Li, C.-H. Lu and H.-H. Yang, High-efficiency X-ray luminescence in Eu^{3+}-activated tungstate nanoprobes for optical imaging through energy transfer sensitization, *Nanoscale*, 2018, **10**, 1607–1612.

12 B. Grabmaier, W. Rossner and J. Leppert, Ceramic scintillators for X-Ray computed tomography, *Phys. Status Solidi A*, 1992, **130**, K183–K187.

13 C. Greskovich and S. Duclos, Ceramic scintillators, *Annu. Rev. Mater. Sci.*, 1997, **27**, 69–88.

14 G. Buşe, A. Giuliani, P. De Marcillac, S. Marnieros, C. Nones, V. Novati, E. Olivieri, D. Poda, T. Redon and J.-B. Sand, First scintillating bolometer tests of a CLYMENE R&D on Li_2MoO_4 scintillators towards a large-scale double-beta decay experiment, *Nucl. Instrum. Methods Phys. Res., Sect. A*, 2018, **891**, 87–91.

15 M. Zhu, H. Qi, M. Pan, Q. Hou, B. Jiang, Y. Jin, H. Han, Z. Song and H. Zhang, Growth and luminescent properties of Yb:YAG and Ca co-doped Yb:YAG ultrafast scintillation crystals, *J. Cryst. Growth*, 2018, **490**, 51–55.
16 V. Bachmann, C. Ronda, O. Oeckler, W. Schnick and A. Meijerink, Color point tuning for $(Sr,Ca,Ba)Si_2O_2N_2:Eu^{2+}$ for white light LEDs, *Chem. Mater.*, 2008, **21**, 316–325.
17 M. A. Lim, J. K. Park, C. H. Kim, H. D. Park and M. W. Han, Luminescence characteristics of green light emitting $Ba_2SiO_4:Eu^{2+}$ phosphor, *J. Mater. Sci. Lett.*, 2003, **22**, 1351–1353.
18 J. Li, Q. Liang, Y. Cao, J. Yan, J. Zhou, Y. Xu, L. Dolgov, Y. Meng, J. Shi and M. Wu, Layered Structure Produced Nonconcentration Quenching in a Novel Eu^{3+}-Doped Phosphor, *ACS Appl. Mater. Interfaces*, 2018, **10**, 41479–41486.
19 M. Janulevicius, P. Marmokas, M. Misevicius, J. Grigorjevaite, L. Mikoliunaite, S. Sakirzanovas and A. Katelnikovas, Luminescence and luminescence quenching of highly efficient $Y_2Mo_4O_{15}:Eu^{3+}$ phosphors and ceramics, *Sci. Rep.*, 2016, **6**, 26098.
20 D. Dexter and J. H. Schulman, Theory of concentration quenching in inorganic phosphors, *J. Chem. Phys.*, 1954, **22**(6), 1063–1070.
21 K. Takahashi, H. Oka and S. Ohnuki, Selective Growth of Noble Gases at Metal/Oxide Interface, *ACS Appl. Mater. Interfaces*, 2016, **8**(6), 3725–3729.
22 Y. K. Liao, D. Y. Jiang, Y. M. Ji and J. L. Shi, in *Combustion synthesis of nanosized $Y_2Hf_2O_7$ and $Lu_2Hf_2O_7$ powders*, Key Engineering Materials, Trans Tech Publ, 2005, pp. 643–646.
23 B.-Z. Zhou, G.-H. Zhou, L.-Q. An, F. Zhang, G.-J. Zhang and S.-W. Wang, Morphology-controlled synthesis of yttrium hafnate by oxalate co-precipitation method and the growth mechanism, *J. Alloys Compd.*, 2009, **481**(1–2), 434–437.
24 Z. Zhang, M. Avdeev, M. de los Reyes, G. R. Lumpkin, B. J. Kennedy, P. E. Blanchard, S. Liu, A. Tadich and B. C. Cowie, Probing Long-and Short-Range Disorder in $Y_2Ti_{2-x}Hf_xO_7$ by Diffraction and Spectroscopy Techniques, *J. Phys. Chem. C*, 2016, **120**, 26465–26479.
25 Y. Cun, Z. Yang, J. Liao, J. Qiu, Z. Song and Y. Yang, Enhancement of upconversion luminescence of three-dimensional ordered macroporous $Bi_2Ti_2O_7:Er^{3+},Yb^{3+}$ by co-doping of Li^+ ions, *Mater. Lett.*, 2014, **131**, 154–157.
26 S. K. Gupta, K. Sudarshan, A. K. Yadav, R. Gupta, D. Bhattacharyya, S. N. Jha and R. M. Kadam, Deciphering the Role of Charge Compensator in Optical Properties of $SrWO_4:Eu^{3+}:A$ ($A = Li^+,Na^+,K^+$): Spectroscopic Insight Using Photoluminescence, Positron Annihilation, and X-ray Absorption, *Inorg. Chem.*, 2018, **57**, 821–832.
27 P. Sobierajska, R. Pazik, K. Zawisza, G. Renaudin, J.-M. Nedelec and R. J. Wiglusz, Effect of lithium substitution on the charge compensation, structural and luminescence properties of nanocrystalline $Ca_{10}(PO_4)_6F_2$ activated with Eu^{3+} ions, *CrystEngComm*, 2016, **18**, 3447–3455.
28 S. Du, D. Wang, Q. Qiang, X. Ma, Z. Tang and Y. Wang, The dual-model up/down-conversion green luminescence of $Gd_6O_5F_8$: Yb^{3+},Ho^{3+},Li^+ and its application for temperature sensing, *J. Mater. Chem. C*, 2016, **4**(29), 7148–7155.
29 S. K. Gupta, K. Sudarshan, P. S. Ghosh, A. P. Srivastava, S. Bevara, P. K. Pujari and R. M. Kadam, Role of various defects in the photoluminescence characteristics of nanocrystalline $Nd_2Zr_2O_7$: an investigation through spectroscopic and DFT calculations, *J. Mater. Chem. C*, 2016, **4**, 4988–5000.
30 S. K. Gupta, J. P. Zuniga, P. S. Ghosh, M. Abdou and Y. Mao, Correlating Structure and Luminescence Properties of Undoped and Eu^{3+}-Doped $La_2Hf_2O_7$ Nanoparticles Prepared with Different Coprecipitating pH Values through Experimental and Theoretical Studies, *Inorg. Chem.*, 2018, **57**, 11815–11830.
31 N. Pathak, P. S. Ghosh, S. K. Gupta, S. Mukherjee, R. M. Kadam and A. Arya, An Insight into the Various Defects-Induced Emission in $MgAl_2O_4$ and Their Tunability with Phase Behavior: Combined Experimental and Theoretical Approach, *J. Phys. Chem. C*, 2016, **120**(7), 4016–4031.
32 S. K. Gupta, P. S. Ghosh, A. K. Yadav, S. N. Jha, D. Bhattacharyya and R. M. Kadam, Origin of Blue-Green Emission in α-$Zn_2P_2O_7$ and Local Structure of Ln^{3+} Ion in α-$Zn_2P_2O_7:Ln^{3+}$ (Ln = Sm, Eu): Time-Resolved Photoluminescence, EXAFS, and DFT Measurements, *Inorg. Chem.*, 2017, **56**, 167–178.
33 T. Du and O. J. Ilegbusi, Synthesis and morphological characterization on PVP/ZnO nano hybrid films, *J. Mater. Sci.*, 2004, **39**, 6105–6109.
34 J. Prakash, V. Kumar, L. J. B. Erasmus, M. M. Duvenhage, G. Sathiyan, S. Bellucci, S. Sun and H. C. Swart, Phosphor Polymer Nanocomposite: $ZnO:Tb^{3+}$ Embedded Polystyrene Nanocomposite Thin Films for Solid-State Lighting Applications, *ACS Appl. Nano Mater.*, 2018, **1**, 977–988.
35 S. K. Gupta, M. Abdou, P. S. Ghosh, J. P. Zuniga and Y. Mao, Thermally Induced Disorder–Order Phase Transition of $Gd_2Hf_2O_7:Eu^{3+}$ Nanoparticles and Its Implication on Photo- and Radioluminescence, *ACS Omega*, 2019, **4**, 2779–2791.
36 S. K. Gupta, M. Abdou, J. P. Zuniga, P. S. Ghosh, E. Molina, B. Xu, M. Chipara and Y. Mao, Roles of oxygen vacancies and pH induced size changes on photo- and radioluminescence of undoped and Eu^{3+}-doped $La_2Zr_2O_7$ nanoparticles, *J. Lumin.*, 2019, **209**, 302–315.
37 M. Pokhrel, M. G. Brik and Y. Mao, Particle Size and Crystal Phase Dependent Photoluminescence of $La_2Zr_2O_7:Eu^{3+}$ Nanoparticles, *J. Am. Ceram. Soc.*, 2015, **98**(10), 3192–3201.
38 M. Pokhrel, K. Wahid and Y. Mao, Systematic Studies on $RE_2Hf_2O_7$:5%Eu^{3+} (RE = Y, La, Pr, Gd, Er, and Lu) Nanoparticles: Effects of the A-Site RE^{3+} Cation and Calcination on Structure and Photoluminescence, *J. Phys. Chem. C*, 2016, **120**, 14828–14839.
39 Y. Eagleman, M. Weber and S. Derenzo, Luminescence study of oxygen vacancies in lanthanum hafnium oxide, $La_2Hf_2O_7$, *J. Lumin.*, 2013, **137**, 93–97.

40 X. Bai, A. Pucci, V. T. Freitas, R. A. Ferreira and N. Pinna, One-step synthesis and optical properties of benzoate- and biphenolate-capped ZrO_2 nanoparticles, *Adv. Funct. Mater.*, 2012, **22**, 4275–4283.

41 E. Rauwel, A. Galeckas and P. Rauwel, Photoluminescent cubic and monoclinic HfO_2 nanoparticles: effects of temperature and ambient, *Mater. Res. Express*, 2014, **1**, 015035.

42 T. Perevalov, V. S. Aliev, V. Gritsenko, A. Saraev, V. Kaichev, E. Ivanova and M. Zamoryanskaya, The origin of 2.7 eV luminescence and 5.2 eV excitation band in hafnium oxide, *Appl. Phys. Lett.*, 2014, **104**, 071904.

43 S. K. Gupta, K. Sudarshan, P. Ghosh, A. Srivastava, S. Bevara, P. Pujari and R. Kadam, Role of various defects in the photoluminescence characteristics of nanocrystalline $Nd_2Zr_2O_7$: an investigation through spectroscopic and DFT calculations, *J. Mater. Chem. C*, 2016, **4**, 4988–5000.

44 S. K. Gupta, P. S. Ghosh, C. Reghukumar, N. Pathak and R. M. Kadam, Experimental and theoretical approach to account for green luminescence from $Gd_2Zr_2O_7$ pyrochlore: exploring the site occupancy and origin of host-dopant energy transfer in $Gd_2Zr_2O_7$:Eu^{3+}, *RSC Adv.*, 2016, **6**, 44908–44920.

45 S. K. Gupta, K. Sudarshan, P. Ghosh, A. Srivastava, S. Bevara, P. Pujari and R. Kadam, Role of various defects in the photoluminescence characteristics of nanocrystalline $Nd_2Zr_2O_7$: an investigation through spectroscopic and DFT calculations, *J. Mater. Chem. C*, 2016, **4**, 4988–5000.

46 A. Huignard, T. Gacoin and J.-P. Boilot, Synthesis and Luminescence Properties of Colloidal YVO_4:Eu Phosphors, *Chem. Mater.*, 2000, **12**(4), 1090–1094.

47 Z. Wei, L. Sun, C. Liao, C. Yan and S. Huang, Fluorescence intensity and color purity improvement in nanosized YBO_3: Eu, *Appl. Phys. Lett.*, 2002, **80**(8), 1447–1449.

48 S. Wen, J. Zhou, K. Zheng, A. Bednarkiewicz, X. Liu and D. Jin, Advances in highly doped upconversion nanoparticles, *Nat. Commun.*, 2018, **9**(1), 2415.

49 G. Blasse, Energy transfer in oxidic phosphors, *Phys. Lett. A*, 1968, **28**, 444–445.

50 Y. Xu, X. Zhang, S. Dai, B. Fan, H. Ma, J.-l. Adam, J. Ren and G. Chen, Efficient Near-Infrared Down-Conversion in Pr^{3+}–Yb^{3+} Codoped Glasses and Glass Ceramics Containing LaF_3 Nanocrystals, *J. Phys. Chem. C*, 2011, **115**(26), 13056–13062.

51 M. Pokhrel, M. G. Brik and Y. Mao, Particle Size and Crystal Phase Dependent Photoluminescence of $La_2Zr_2O_7$: Eu^{3+} Nanoparticles, *J. Am. Ceram. Soc.*, 2015, **98**(10), 3192–3201.

52 I. Ahemen, F. B. Dejene, R. E. Kroon and H. C. Swart, Effect of europium ion concentration on the structural and photoluminescence properties of novel Li_2BaZrO_4:Eu^{3+} nanocrystals, *Opt. Mater.*, 2017, **74**, 58–66.

53 C.-C. Hsu, S.-L. Lin and C. A. Chang, Lanthanide-Doped Core–Shell–Shell Nanocomposite for Dual Photodynamic Therapy and Luminescence Imaging by a Single X-ray Excitation Source, *ACS Appl. Mater. Interfaces*, 2018, **10**, 7859–7870.

54 S. K. Gupta, P. S. Ghosh, A. K. Yadav, S. N. Jha, D. Bhattacharyya and R. M. Kadam, Origin of blue-green emission in α-$Zn_2P_2O_7$ and local structure of Ln^{3+} Ion in α-$Zn_2P_2O_7$:Ln (Ln = Sm, Eu): Time-resolved photoluminescence, EXAFS, and DFT measurements, *Inorg. Chem.*, 2016, **56**, 167–178.

55 S. K. Gupta, M. Mohapatra, S. Godbole and V. Natarajan, On the unusual photoluminescence of Eu^{3+} in α-$Zn_2P_2O_7$: a time resolved emission spectrometric and Judd–Ofelt study, *RSC Adv.*, 2013, **3**, 20046–20053.

56 S. K. Mahesh, P. P. Rao, M. Thomas, T. L. Francis and P. Koshy, Influence of Cation Substitution and Activator Site Exchange on the Photoluminescence Properties of Eu^{3+}-Doped Quaternary Pyrochlore Oxides, *Inorg. Chem.*, 2013, **52**, 13304–13313.

57 J. Papan, D. J. Jovanović, K. Vuković, K. Smits, V. Đorđević and M. Dramićanin, Europium(III)-doped $A_2Hf_2O_7$ (A = Y, Gd, Lu) nanoparticles: Influence of annealing temperature, europium(III) concentration and host cation on the luminescent properties, *Opt. Mater.*, 2016, **61**, 68–76.

58 D. Prakashbabu, H. B. Ramalingam, R. Hari Krishna, B. M. Nagabhushana, R. Chandramohan, C. Shivakumara, J. Thirumalai and T. Thomas, Charge compensation assisted enhancement of photoluminescence in combustion derived Li^+ co-doped cubic ZrO_2:Eu^{3+} nanophosphors, *Phys. Chem. Chem. Phys.*, 2016, **18**, 29447–29457.

59 N. Jain, R. Paroha, R. K. Singh, S. K. Mishra, S. K. Chaurasiya, R. A. Singh and J. Singh, Synthesis and Rational design of Europium and Lithium Doped Sodium Zinc Molybdate with Red Emission for Optical Imaging, *Sci. Rep.*, 2019, **9**, 2472.

60 R. G. A. Kumar, S. Hata, K.-i. Ikeda and K. G. Gopchandran, Organic mediated synthesis of highly luminescent Li^+ ion compensated Gd_2O_3:Eu^{3+} nanophosphors and their Judd–Ofelt analysis, *RSC Adv.*, 2016, **6**, 67295–67307.

61 M. Puchalska and E. Zych, The effect of charge compensation by means of Na^+ ions on the luminescence behavior of Sm^{3+}-doped $CaAl_4O_7$ phosphor, *J. Lumin.*, 2012, **132**, 826–831.

62 D. Avram, B. Cojocaru, I. Tiseanu, M. Florea and C. Tiseanu, Down-/Up-Conversion Emission Enhancement by Li Addition: Improved Crystallization or Local Structure Distortion?, *J. Phys. Chem. C*, 2017, **121**, 14274–14284.

63 I. N. Stanton, M. D. Belley, G. Nguyen, A. Rodrigues, Y. Li, D. G. Kirsch, T. T. Yoshizumi and M. J. Therien, Europium- and lithium-doped yttrium oxide nanocrystals that provide a linear emissive response with X-ray radiation exposure, *Nanoscale*, 2014, **6**(10), 5284–5288.

64 R. Cao, G. Chen, X. Yu, C. Cao, K. Chen, P. Liu and S. Jiang, Luminescence properties of $Ca_3Ti_2O_7$:Eu^{3+},Bi^{3+}, R+ (R^+=Li^+, Na^+, and K^+) red emission phosphor, *J. Solid State Chem.*, 2014, **220**, 97–101.

65 O. A. Lopez, J. McKittrick and L. E. Shea, Fluorescence properties of polycrystalline Tm^{3+}-activated $Y_3Al_5O_{12}$ and Tm^{3+}-Li^+ co-activated $Y_3Al_5O_{12}$ in the visible and near IR ranges, *J. Lumin.*, 1997, **71**, 1–11.

66 B. P. Singh, A. K. Parchur, R. S. Ningthoujam, P. V. Ramakrishna, S. Singh, P. Singh, S. B. Rai and R. Maalej, Enhanced up-conversion and temperature-sensing behaviour of Er^{3+} and Yb^{3+} co-doped $Y_2Ti_2O_7$ by incorporation of Li^+ ions, *Phys. Chem. Chem. Phys.*, 2014, **16**, 22665–22676.
67 S. K. Gupta, K. Sudarshan, A. K. Yadav, R. Gupta, D. Bhattacharyya, S. N. Jha and R. M. Kadam, Deciphering the role of charge compensator in optical properties of $SrWO_4$:Eu^{3+}:A (A = Li^+, Na^+, K^+): Spectroscopic insight using photoluminescence, positron annihilation, and X-ray absorption, *Inorg. Chem.*, 2018, **57**, 821–832.
68 B. L. Abrams and P. H. Holloway, Role of the Surface in Luminescent Processes, *Chem. Rev.*, 2004, **104**, 5783–5802.
69 J. S. Bae, J. H. Yoon, S. K. Park, J. P. Kim, E. D. Jeong, M. S. Won, J. H. Jeong, K. S. Shim, H. K. Yang and S. S. Yi, Li-Doping effect on the cathodoluminescent properties of Y_2O_3:Eu^{3+} phosphors, *Surf. Rev. Lett.*, 2007, **14**, 535–538.